PAPER • OPEN ACCESS

Highly porous tungsten for plasma-facing applications in nuclear fusion power plants: a computational analysis of hollow nanoparticles

View the article online for updates and enhancements.

Highly porous tungsten for plasma-facing applications in nuclear fusion power plants: a computational analysis of hollow nanoparticles

Pablo Díaz-Rodríguez[1,a] **, Francisco Munoz**[2,3] **, José Rogan**[2,3] **, Ignacio Martín-Bragado**[4] **, J.M. Perlado**[1,5] **, Ovidio Peña-Rodríguez**[1,5] **, Antonio Rivera**[1,5] **and Felipe J. Valencia**[3,6]

[1] Instituto de Fusión Nuclear 'Guillermo Velarde', Universidad Politécnica de Madrid, Spain
[2] Departamento de Física, Facultad de Ciencias, Universidad de Chile, Casilla 653, Santiago 7800024, Chile
[3] Centro para el Desarrollo de la Nanociencia y la Nanotecnología (CEDENNA), Universidad de Santiago de Chile, USACH, Av. Ecuador, 3493, Santiago, Chile
[4] Universidad Católica de Murcia – Campus de los Jerónimos, Murcia, Spain
[5] Departamento de Ingeniería Energética, ETSI Industriales, Universidad Politécnica de Madrid, Spain
[6] DAiTA Lab, Facultad de Ciencias, Universidad Mayor, Chile

E-mail: p.diazr@upm.es

CrossMark

Abstract

Plasma-facing materials (PFMs) for nuclear fusion, either in inertial confinement fusion (ICF) or in magnetic confinement fusion (MCF) approaches, must withstand extremely hostile irradiation conditions. Mitigation strategies are plausible in some cases, but usually the best, or even the only, solution for feasible plant designs is to rely on PFMs able to tolerate these irradiation conditions. Unfortunately, many studies report a lack of appropriate materials that have a good thermomechanical response and are not prone to deterioration by means of irradiation damage. The most deleterious effects are vacancy clustering and the retention of light species, as is the case for tungsten. In an attempt to find new radiation-resistant materials, we studied tungsten hollow nanoparticles under different irradiation scenarios that mimic ICF and MCF conditions. By means of classical molecular dynamics, we determined that these particles can resist astonishingly high temperatures (up to $\sim$3000 K) and huge internal pressures (>5 GPa at 3000 K) before rupture. In addition, in the case of gentle pressure increase (ICF scenarios), a self-healing mechanism leads to the formation of an opening through which gas atoms are able to escape. The opening disappears as the pressure drops, restoring the original particle. Regarding radiation damage, object kinetic Monte Carlo simulations show an additional self-healing mechanism. At the temperatures of interest, defects (including clusters) easily reach the nanoparticle surface and disappear, which makes the hollow nanoparticles promising for ICF designs. The situation is less promising for MCF because the huge ion densities expected at the surface of PFMs lead to inevitable particle rupture.

[a] Author to whom any correspondence should be addressed.

(Some figures may appear in colour only in the online journal)

1. Introduction

The development of nuclear fusion power plants is limited by a number of bottlenecks [1–3]. In recent decades, the scientific communities working on magnetic confinement fusion (MCF) and inertial confinement fusion (ICF) have made important efforts to overcome these issues. One of the limiting factors is the lack of appropriate plasma-facing materials (PFMs) (see [2–6] and references therein) able to withstand the harsh irradiation conditions, particularly the high temperatures and atomistic damage levels reached under pulsed irradiation events in both ICF and MCF [5, 7]. Different engineering solutions have been proposed for plasma-facing applications. The very existence of some of these projects is often seen as the only way to bridge gaps that otherwise would be naturally resolved by the use of appropriate materials. It is not our intention to dismiss engineering solutions; for certain problems they are the optimal solution. Even the most unorthodox projects constitute an expression of the need for solutions to overcome the lack of suitable PFMs. However, true solutions must properly address cost, complexity and actual performance, and not only partial aspects of these.

An example of an optimal engineering solution is the use of a buffer gas to mitigate the arrival of ions and intense x-ray pulses to the chamber walls in ICF plants with indirect-drive targets [8, 9]. There are some concerns about harm due to shrapnel (large neutral clusters with hyper-velocities) in these plants [10], which are more serious for the final optics than for the chamber walls. Otherwise, if shrapnel effects could be ignored the buffer gas solution would relax the irradiation conditions at the chamber walls to the extent that even bare steel could survive. In the case of ICF with direct-drive targets, shrapnel is not a concern, but the buffer gas is incompatible with target cryogenics during injection [11]. Alternative solutions [12] have been proposed, such as magnetic intervention [13] or wetted wall concepts [14, 15]. Many years after the first proposals of wetted walls [16], aspects like the formation of aerosols, the vapour pressure inside the chamber or the maintenance of a liquid layer over all the internal surfaces of the chamber remain unaddressed [17], despite their paramount importance for this approach. Indeed, aerosols may preclude the propagation of the laser beam, the vapour pressure may prevent the target injection and a poor protection of all the internal surfaces goes against the first goal of the wetted wall projects, *i.e.* to protect the chamber materials against irradiation. Obviously, for ICF power plants, appropriate PFMs would solve a long-standing problem that is difficult to tackle otherwise. On the other hand, in MCF concepts, the divertor is expected to suffer the most hostile conditions, complicating the survival of a solid divertor. This has led to proposals based on the use of liquid materials [18]. An extensive validation of all the relevant aspects of these designs is under way.

Tungsten is considered the most promising candidate for plasma-facing applications [19, 20] due to its high melting temperature and hardness, low chemical sputtering yield, and good thermal conductivity. However, despite these remarkable properties, the performance of W is compromised when facing high particle fluxes (typically, higher than 10^{19} cm^{-2} s^{-1}), due to thermomechanical considerations [6], and more importantly, due to atomistic considerations, which are behind a myriad of detrimental effects such as blistering, swelling and fuzz formation [19, 21, 22]. The origin of the atomistic effects is the nucleation of light species (mainly He and H) in point defects. The role of He is particularly relevant due to its low solubility and high binding energy to vacancy-type defects [23]. Moreover, He clustering is energetically favourable and possible due to its high mobility [24]. Vacancy clusters may accumulate He atoms until, at high enough temperatures, the generation of open volume by the creation of Frenkel pairs becomes energetically favourable. The highly mobile interstitial atoms easily escape, and the vacancy is retained in ever-growing vacancy clusters able to accommodate the excess of He. Thus, these clusters are unwanted bubble precursors. From the mechanical point of view, the presence of bubbles is associated with high local stress fields and dislocation loop nucleation, with fatal effects on the mechanical performance, such as embrittlement, which is especially relevant in a material as brittle as W. Suppressing the formation of vacancy clusters contributes to improving the resistance of PFMs.

Different strategies have been proposed to overcome this situation. Many of them are based on finding materials or configurations with self-healing properties, *i.e.* able to eliminate spontaneously the deleterious effects of irradiation [25]. Some studies focus on materials with a high density of grain boundaries to promote the annealing of point defects [26], enhanced under certain conditions [27]. This approach showed promising results for the annihilation of self-defects and the release of hydrogen isotopes [28] but, as in the case of bulk W, does not solve the problem of He retention because the grain boundaries do not favour He release [29, 30]. A related approach is based on the development of engineered surfaces with a large surface area to distribute the heat loads along the material. This has been achieved by fabricating microstructures such as dendrites, needles or foams at the surface of the PFMs. These structures have the added advantage that they contribute to release light species and annihilate self-defects, enhancing the self-healing properties of the material [31–34]. Irradiation tests in conditions similar to those expected in real facilities are essential to attain useful conclusions about the different strategies for materials development. For example, realistic irradiations were carried out in a dedicated facility (RHEPP, Sandia National Laboratories, NM, USA) [31–34], appropriate to mimic first wall (FW) irradiation conditions in ICF plants. Thus, the authors showed that the development

of engineered surfaces has a positive impact on the materials response to ICF conditions. Unfortunately for the ICF community, RHEPP is now dismantled, and nowadays useful validation tests demand the adaptation of facilities that were not originally designed for ICF studies and the use of sophisticated modelling methods to extract useful conclusions.

Surface microstructures have also been studied under MCF conditions and, although in this case there exist more irradiation facilities, the high fluxes of low-energy ions complicate the development of a solid material able to withstand the irradiation conditions. Nonetheless, recent works report on significant improvements for micro-modified surfaces [35, 36]. Further size reduction from the micrometre to the nanometre level has been explored, and nanostructured materials are regarded as a viable alternative to prevent He accumulation and the associated bubble growth [37–40]. The key advantage of nanostructured materials is that the surfaces and grain boundaries act as sinks for defects. In these materials, defects easily annihilate at the abundant annihilation sites located within the mean free path of mobile defects. Thus, defect evolution in nanostructured materials is considerably faster than in microstructured materials and it is completely different with respect to that in their bulk counterparts. The most important consequence is the efficient reduction of nucleation sites, *i.e.* clustering precursors. Indeed, some works have exploited defect sinks to reduce the number of nucleation sites, with promising results. Recently, Qin *et al* [37] explored a nanochannel design as a route to delay He bubble growth in W. They found a decrease of 50% in the fuzz formation when compared with the bulk case. A similar approach employs carbon nanotube inclusions [39]. Other works showed that W nanoparticles (NPs) with a high surface-to-volume ratio have enhanced radiation tolerance, strongly related to the NP size [38, 41]. Many of the current efforts require validation tests in well-defined irradiation conditions to extract useful conclusions. These tests are difficult to perform for a number of reasons, and the lack of dedicated facilities for ICF irradiations is not the only problem. A correct identification of the irradiation conditions and subsequent mimicking in an irradiation facility is not straightforward, even when dedicated facilities are available, as is the case for MCF. In addition, the fabrication of nanostructured samples is in some cases done by state-of-the-art nanotechnology techniques, which typically produce tiny samples on delicate substrates not designed for extreme irradiation. In this sense, modelling reports (such as this paper) provide useful insight into possible pathways to explore in order to develop new PFMs.

Nanostructuring approaches suggest that highly porous materials—combining migration channels, short diffusion paths, high surface areas, and several recombination sinks—are promising alternatives to avoid He accumulation. In recent years, hollow nanospheres (hNPs), a new kind of low-density nanomaterial, have been synthesized. They are composed of a thin shell enclosing an empty cavity (core). The existence of a cavity inside the NP has been exploited for gas storage purposes, offering a great performance in energy devices. In addition, these structures exhibit an improvement in the mechanical stability due to their convenient combination of

strength and flexibility [42–45], and a considerable enhancement in the kinetics of defect annihilation [46, 47]. Thus, the use of tungsten hollow nanoparticles (W-hNPs) to fabricate the outer layer of a plasma-facing component is attractive for several reasons: (i) point defects generated by light species in the W-hNP shell will easily reach the surface and annihilate; (ii) light species will easily reach either the outer surface and desorb or the inner surface and accumulate in the cavity; and (iii) the existence of pressurized gas trapped in the cavity contributes to stopping the incoming ions without negative effects for the W-hNPs.

In this paper, we explore the behaviour of W-hNPs under realistic irradiation conditions expected in future ICF and MCF facilities. In particular, key aspects like their resistance to high temperature and pressure, release of light species, and defect annihilation are addressed through a combination of molecular dynamics (MD) and object kinetic Monte Carlo (OKMC) simulation methods. With this strategy we can study in detail short-time scales and explore the behaviour of the W-hNP over long irradiation times to estimate: (i) the thermal behaviour to ensure material stability in real nuclear fusion environments; (ii) the effect of the ion flux on the NP integrity and properties (the main difference between the MCF and ICF approaches); and (iii) the time evolution of the generated defects.

We show that W-hNPs may fulfil the stringent requirements of a PFM under ICF conditions due to their remarkable self-healing properties. Therefore, if these findings are confirmed experimentally, the principles behind the good behaviour of W-hNPs could be used to develop the long searched-for PFM for realistic plant designs, which will certainly overcome the drawbacks mentioned above. Regarding MCF conditions, W-hNP behaviour is less promising due to the high ion fluxes expected in discharge events such as edge localized modes (ELMs).

The efforts made towards the development of new materials are highly relevant, since many problems stem from a lack of appropriate materials. This paper is an effort to make progress on materials development for FW applications. Being successful on this front not only solves an existing problem (how to protect the chamber) but does it in the simplest way, avoiding the need for additional efforts to develop complex solutions. It is hoped that our findings will open a new route towards the development of materials for plasma-facing applications with enhanced radiation resistance properties, particularly in terms of irradiation damage.

2. FW made of hollow NPs in different irradiation scenarios

In order to assess the performance of W-hNPs as a PFM, we have identified realistic irradiation scenarios expected in future nuclear fusion facilities. In the case of ICF with indirect-drive targets, a realistic solution is to mitigate the effects of the x-ray pulses on the chamber wall by means of a residual gas in the chamber [8, 9]. With this configuration (ignoring the
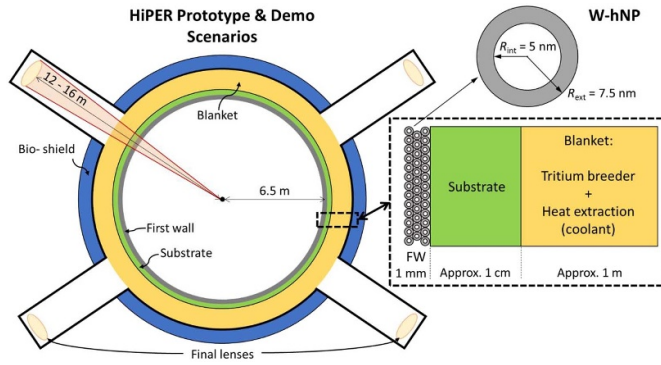
Figure 1. Schematic representation of the HiPER fusion chamber for the *Prototype* and *Demo* scenarios. It is an evacuated dry-walled chamber of radius 6.5 m with 48 square lenses at a distance of 12–16 m from the chamber centre. On the right is a sketch of the wall, which, for the purpose of this work, consists of a FW of W-hNPs, supported on a structural substrate and surrounded by a cooling blanket. A detail of the studied W-hNPs is given top right.

open question of shrapnel threats [10]), the irradiation conditions at the chamber wall are very relaxed, to the extent that even bare steel is expected to survive. Therefore, we do not consider the indirect-drive target scenario here. On the other hand, ICF with direct-drive targets requires a vacuum chamber (schematically shown in figure 1) and a radiation-resistant PFM for the FW to withstand the generated ion pulses. The divertor in MCF will be the component most exposed to potentially fatal irradiation conditions during pulsed events such as ELMs [48].

2.1. Hollow NPs

Our main goal in this paper is to study the performance of a FW made of W-hNPs under different scenarios. The uncertainties in relevant thermal parameters are significant, but we have tried to use realistic values for the irradiation fluxes and chamber dimensions, including a model for the W-hNPs. Thus, we studied W-hNPs with an outer radius of 7.5 nm and inner radius of 5 nm, *i.e.* the shell thickness is 2.5 nm. A compact configuration of NPs (as an fcc arrangement in crystallography) has a density of 10 030 kg m^{-3}, *i.e.* 52% of the bulk tungsten density (19 250 kg m^{-3}). The thermal conductivity of a FW made of these W-hNPs has been conservatively estimated to be 1/3 that of bulk tungsten [49], which agrees well with the values given by Bhatt *et al* [50] for metal NPs. Our calculations assume considerably lower values of thermal conductivity, as shown next. In order to estimate the FW temperature under different irradiation conditions, we solved the 1D heat equation with rough source terms as described below. Further sophistication is meaningless at this point, due to the uncertainties in the thermal parameters. For verification, we used the same rough approach to obtain the temperature evolution of bulk tungsten under irradiation and compared the results with those rigorously calculated in [6], obtaining a satisfactory agreement for the purpose of this work.

2.2. ICF approach with direct-drive targets

For the direct-drive target ICF approach, the scenarios considered in this work are based on the HiPER project [6]. Figure 1 schematically depicts the spherical reaction chamber (radius 6.5 m) and details the wall structure: a FW supported on a structural substrate in contact with the breeding blanket, which also has cooling functions. In an effort to overcome the problems encountered for FWs made of bulk tungsten, we study in this work chambers with a FW composed of W-hNPs. Table 1 shows two scenarios considered here to address the performance of the W-hNPs as a FW material. These scenarios were previously used in the ICF HiPER project [6]. The *'Demo'* scenario is the expected irradiation scenario of a full-scale power plant, whereas the *'Prototype'* scenario is a relaxed mode scenario useful to test plant systems and materials. The major concern regarding the FW is related to the arrival of short and intense ion pulses originated in the target explosions. Ions account for more than 25% of the total energy reaching the FW (neutrons carry most of the generated energy, ~70%). These pulses are responsible for the extreme thermo-mechanical conditions that the FW must face. In addition, ion irradiation is responsible for defect generation and determines the final fate of the material at a microstructural level, eventually with fatal consequences for FWs made of tungsten [6]. According to the irradiation spectra [51], the most important ion contributions stem from fast burn product He ion pulses and slow debris D + T ion pulses (details in table 1). These pulses account for 19% of the total energy deposited in the wall. Since the uncertainties in the thermal parameters of W-hNPs are important, we will ignore other contributions to estimate the temperature and defect evolution of the FW made of W-hNPs, similarly to in [48].

Figure 2 shows the results of simulations obtained with the binary collision approximation (BCA) code SRIM [52, 53] for the irradiation of bulk W and W-hNPs with D and He ions using representative ion energies (300 keV and 2 MeV, respectively) as model cases. The effect of the material mass density can be clearly observed. The implantation and vacancy profiles become broader and reach a maximum deeper in the case of hNPs with an effective mass density of 0.52 that of bulk W. The deposited energy profiles also broaden in the case of hNPs due to the mass density effect. Related to these profiles, we can obtain the maximum implanted ion concentration and vacancy concentration for these irradiation energies (table 1), which, unsurprisingly, are lower for the hNPs than for bulk W. From these values, we can determine the maximum number of He, D + T and vacancies, expected for the considered hNPs (volume 1767.15 nm^3). For example, the maximum number of D + T ions per shot expected in a hNP in the *Demo* scenario is 2.8, and in the *Prototype* scenario it is 0.9.

Both implanted ion concentration and vacancy concentration are lower for hNPs than for bulk W, which in principle favours the use of hNPs. However, this factor is not so determinant as the temperatures reached for both types of walls. The lower thermal conductivity of the FW made of hNPs leads to considerably higher temperatures. Figure 3 shows a rough estimate of the temperature evolution for a FW made of hNPs

Table 1. Irradiation scenarios *Prototype* and *Demo* of the HiPER project [6] considered in this work for ICF power plants with an evacuated chamber of 6.5 m radius.

	Prototype	*Demo*
Yield (MJ)	50	154
Rep. rate (Hz)	1–10	10–20
Power (GW)	<0.5	<1
On FW per shot	–	–
Total energy (J cm^{-2})	9.4	29.0
Debris D + T energy (J cm^{-2})	1.2	3.7
Burn product He energy (J cm^{-2})	0.6	1.8
Debris D + T density (cm^{-2})	4.5×10^{13}	1.4×10^{14}
Burn product He density (cm^{-2})	1.9×10^{12}	5.8×10^{12}
With bulk tungsten[a]	–	–
Max. D + T (10^{16} cm^{-3})	91	280
Max. D + T-induced vacancies (10^{16} cm^{-3})	890	2700
Max. He (10^{16} cm^{-3})	4.2	13
Max. He-induced vacancies (10^{16} cm^{-3})	150	470
With hollow NPs[a,b]	–	–
Max. D + T (10^{16} cm^{-3})	51 (0.9)	160 (2.8)
Max. D + T-induced vacancies (10^{16} cm^{-3})	360 (6.3)	1100 (19.4)
Max. He (10^{16} cm^{-3})	2.4 (0.04)	7.5 (0.1)
Max. He-induced vacancies (10^{16} cm^{-3})	76 (1.3)	230 (4.1)

[a]Model case: 300 keV D and 2 MeV He irradiations.
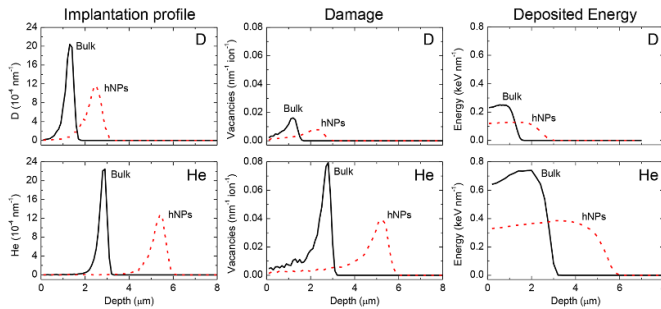[b]In brackets: number per hNP.

Figure 2. Implantation profile, damage generation and deposited energy by irradiation of a FW composed of bulk tungsten or hollow NPs obtained for the following model cases: irradiation with 300 keV D-ions (top row), and with 2 MeV He-ions (bottom row).

under *Demo* and *Prototype* irradiation conditions. For the calculation, we considered that the energy deposited by burn product He and debris D + T ions per time are step functions (source terms of the heat equation). This means that the source terms were just approximations to the deposited energy curves of figure 2, but they provide acceptable results. Both He and D + T temperature peaks exceed the meting point of W in the *Demo* scenario (154 MJ), which invalidates the use of hNPs as FW material in this case. For bulk W, the same scenario leads to temperatures of ∼3400 and ∼2400 K for the He and D + T peaks, respectively [6]. These values are below the melting point of W but, as has been discussed in [6, 54], this is not enough to assure the survival of a FW composed of bulk W. On the other hand, the maximum temperature expected in the *Prototype* scenario, assuming the thermal conductivity of the hNPs to be 1/3 (1/7) of that of bulk tungsten, is
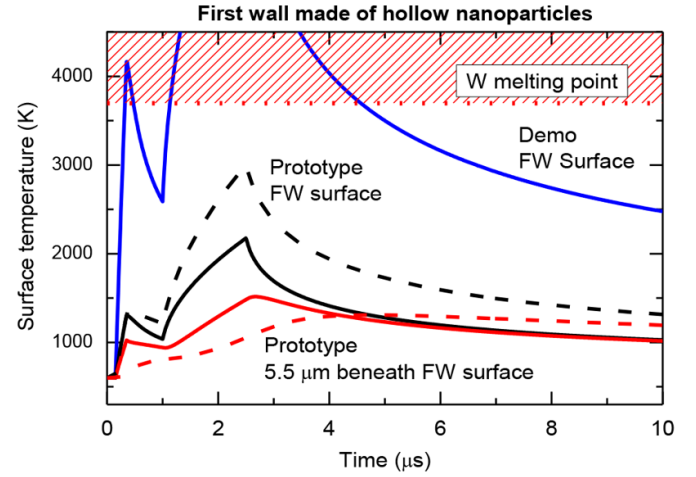

Figure 3. Temperature of a FW made of hollow NPs as a function of time after target explosion ($t = 0$) for target yields of 154 MJ (blue) and 50 MJ (rest), *Demo* and *Prototype* scenarios, respectively. In the *Prototype* scenario, the temperature at the surface (black) and at a depth of 5.5 μm beneath the surface (red) is plotted. Temperatures are estimated by assuming two contributions: a fast burn product He pulse followed by a debris D + T pulse, which results in the two observed peaks. The calculations are done with different effective thermal conductivities, 1/3 and 1/7 of the tungsten thermal conductivity (continuous and dashed lines, respectively). The shaded region is above the melting point of tungsten.

around 2000 K (3000 K) at the FW surface and below 1500 K at 5.5 μm beneath the surface (the region where the maximum concentrations of implanted He ions and induced vacancies are produced, according to figure 2). These values are considerably below the melting point of W, and as discussed in section 4, within the operational temperature limits for hNPs.

2.3. The divertor in the MCF approach

Regarding the MCF approach, the considered scenario corresponds to the conditions found in ITER during an ELM [48]. During this event, particles reach the divertor in 0.2 ms, which is translated to a power density of 5000 MW m^{-2}. The ion energies are below 50 eV, much lower than in the ICF approach. Note that this scenario is based on ITER conditions, which are not actually power-plant conditions. However, the low ion energy leads to a very shallow implantation, which, combined with the high particle fluxes, results in a very high ion density in the mean implantation depth, which is very detrimental for the PFM in the divertor. Figure 4 shows the expected temperature evolution after an ELM discharge onto a W divertor covered with a few layers of hNPs to stop the low-energy ions. With this configuration, we assumed the thermal conductivity of bulk W for the calculations, but even with these relaxed conditions, the temperature exceeds the melting point of W, which certainly compromises the survival of the divertor. In order to complete this study, we considered a relaxed ELM scenario in which only 70% of the actual ELM energy is deposited onto the divertor (*i.e.* 3500 MW m^{-2}). In this case, the expected maximum temperature is slightly over 3000 K. As will be discussed, due to the difficulties found even in
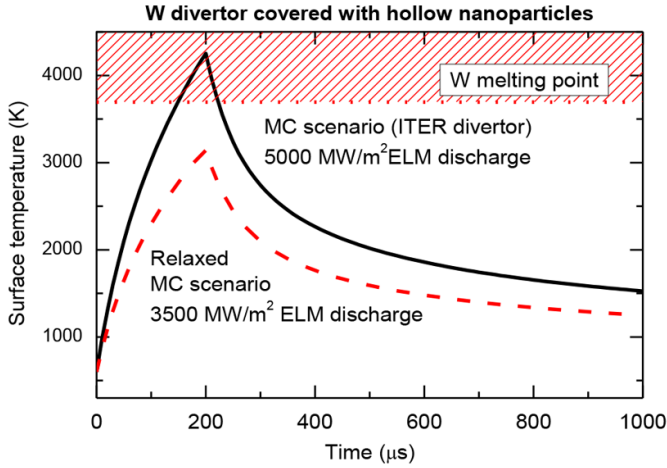
W divertor covered with hollow nanoparticles

Figure 4. Surface temperature of ITER divertor as a function of time after ELM discharge. Two cases were considered: the expected ELM discharge (5000 MW m^{-2}), and a relaxed case with only 70% of the actual power (*i.e.* 3500 MW m^{-2}). The divertor is supposed to be made of tungsten covered with a layer of W-hNPs, thus the thermal conductivity assumed for the calculations was that of bulk tungsten.

this relaxed scenario of ITER, no other MCF scenarios were explored, *i.e.* no realistic power-plant scenarios were taken into account for the MCF approach.

3. Methods

3.1. Atomistic simulations

Atomistic simulations were carried out using the MD code LAMMPS [55]. The W–W interaction was simulated with an embedded atom method potential [56] using the Ackland–Thetford [57] parametrization, together with the modification proposed by Juslin *et al* [58]. For the W–He interaction, we employed the pair potential of Juslin and Wirth [58]. This potential successfully reproduces the formation energy of He atoms in tetrahedral and octahedral sites. Several many-body potentials have been proposed to study He defects and bubble growth in W materials [59, 60]. Among them, the Juslin potential shows a good agreement with density functional theory (DFT) calculations for the binding energy of He clusters of sizes relevant to our study. Finally, the He–He interaction was simulated by using the Beck potential [61]. In all cases, the short-range interaction for each interatomic potential was splined with the Ziegler–Biersack–Littmark (ZBL) potential [62].

The W-hNPs were created from <100> W bulk, by cutting two concentric spheres of 5.0 and 7.5 nm radius. The resulting W-hNP is perfectly crystalline, with an outer radius and thickness of 7.5 nm and 2.5 nm, respectively (figure 1). This procedure has been used to describe the stability of W-hNPs [47, 63, 64], showing a good agreement with experimental results. The W-hNPs were relaxed by annealing to remove any residual stress [63]. For the study of thermal stability, the W-hNP temperature was raised from 300 to 3000 K in steps of 20 K every

0.2 ns, by means of a Nose–Hoover thermostat with a 1 fs time step. Once the W-hNP was relaxed, the nanostructure was irradiated with He ions in the range from 50 to 200 eV. At this stage we kept the W-hNP temperature constant at 300 K. He ions impinged onto random surface positions but targeting the W-hNP centre. During the irradiation, an adaptive time step ranging from 0.001 to 1.0 fs was chosen to avoid problems with energy conservation due to the high-energy collisions.

To study the capacity of the hNP to retain He in the inner cavity, He atoms were continuously inserted every ∼20 ps, up to a maximum limit of 52 100 He atoms. This simulation was performed at 300, 1000, 2000 and 3000 K, using a Nose–Hoover thermostat and an adaptive time step ranging from 0.1 to 1.0 fs. After the hNP rupture due to the He gas pressure, the dynamics was followed during 50 ns to observe whether the remaining structure ende up collapsing or the spherical geometry was successfully preserved.

To compute the gas pressure and the system stresses, we calculate the per-atom stress of the atom α using the virial stress tensor

$$\sigma_{ij}^{\alpha} = \frac{1}{V_{\alpha}} \left[\frac{1}{2} \sum \left(r_i^{\beta} - r_j^{\alpha} \right) F_i^{\alpha\beta} + m^{\alpha} v_i^{\alpha} v_j^{\alpha} \right], \qquad (1)$$

where the subscripts i and j refer to the x, y, or z direction, and m^{α} refers to the mass of the atom α. The v_i^{α} and v_j^{α} terms correspond to the i, j components of the velocity. The first term of the equation represents the elastic strain defined by the component i of the force between the α atom and its neighbour atom β ($F_i^{\alpha\beta}$), and the β index ranges from 1 to N, where N is the number of neighbours of the atom α. r_i^{α} and r_j^{β} correspond to the components i, j of the position for both α and β atoms, respectively. The term V_{α} represents the atomic volume of the atom α. To compute the He gas pressure, the atomic volume was calculated assuming the He van der Waals radii, $R = 1.4$ Å. Based on the virial stress tensor the atomic pressure of α, p^{α}, can be obtained as:

$$p^{\alpha} = \frac{\left(\sigma_{xx}^{\alpha} + \sigma_{yy}^{\alpha} + \sigma_{zz}^{\alpha} \right)}{3}. \qquad (2)$$

Defect identification was performed using the polyhedral template matching method [65], and defect identification, post-processing and visualization were carried out with OVITO software [66, 67].

3.2. OKMC simulations

whereas the time scale of irradiation events is achievable by MD simulations, defect evolution and He diffusion are computationally very expensive to simulate due to the long characteristic time scales. Therefore, a multi-scale approach based on MD and OKMC simulations was followed to simulate long-time dynamical features. The intrinsic characteristics of OKMC methods makes them an attractive option to simulate defect evolution in realistic geometries, being able to access long time periods (from nanoseconds to hours). Following this multi-scale approach, OKMC simulations were performed to study the evolution of the damage cascades produced in the

different ICF and MCF irradiation scenarios. OKMC simulations were performed with the Open Source MMonCa code [68]. This code has been parametrized by means of DFT calculations to simulate the irradiation and defect evolution in different refractory materials. More specifically, in W–He systems, MMonCa has been used as a tool to understand the microscale behaviour of clustering and fuzz formation, providing good agreement with previous experimental reports [69, 70]. The code takes into account the migration of point defects, He, vacancies (V), self-interstitials (I) and vacancies with one He atom (HeV). Cluster formation is also considered, including pure helium clusters, He_n, mixed clusters with vacancies, He_nV_m, and with self-interstitial atoms, He_nI_m. Details on the parametrization can be found elsewhere [71, 72]. A W-hNP such as the one shown in figure 1 was used for the simulations. Damage cascades produce by He irradiation were obtained with SRIM [52, 53] for the different irradiation scenarios. Due to the large He formation energy in W (around 6 eV), the inner and outer surfaces of the W-hNP were considered to be desorption surfaces. Regarding point defects, they act as perfect sinks, *i.e.* point defects reaching the surfaces were removed from the simulation. We took into account the number of He atoms reaching the inner cavity in order to quantify the inner pressure. Several OKMC simulations (with different random seed) were performed for each irradiation scenario (at least 20) to minimize artefacts.

4. Results

4.1. Temperature and pressure effects on hollow NPs

A minimal requirement for a nanostructured material such as W-hNP to be useful as a PFM is structural stability at high temperatures. In W-hNP, the cavity introduces an additional degree of freedom, leading to a structural collapse driven by the surface diffusion of the inner wall. Hence, the temperature resistance of W-hNP with respect to bulk materials is lowered [73]. Our MD simulations of the potential energy, as a function of temperature, show the first structural transition near to 3000 K (figure 5). When dealing with NPs, this transition is usually associated with the melting point, but in the specific case of W-hNPs, the first drop corresponds to the partial collapse or shrinkage of the hollow nanostructure (figure 5(*b*)), as has been reported by Huang *et al* [73]. At higher temperatures the W-hNP fully collapses into a solid NP, and finally melts at 3500 K. Even though the W-hNP has its first (partial) structural transition at 2700 K it remains somewhat stable up to at least 3000 K, a value astonishingly close to the melting point of bulk W. Note that the results shown in figure 5 were obtained for an empty W-hNP. As shown below, a more realistic situation with a pressurized W-hNP leads to a reduced trend to collapse. A structural analysis using the polyhedral template matching method reveals that these W-hNPs preserve their bcc structure, radius and spherical shape at temperatures beyond the typical experimental conditions of a PFM. Its underlying bcc lattice,
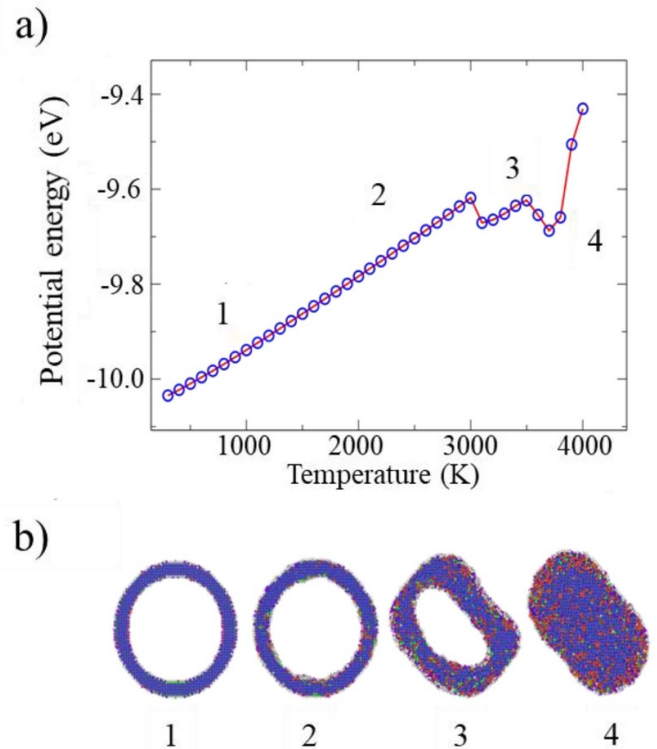

Figure 5. (a) Potential energy per atom for a hollow NP as a function of the temperature. Numbers 1–4 indicate the corresponding snapshots in (b), which represent a cross section of 1 nm thickness. Colours represent the local atomic structure obtained with the polyhedral template matching method. Blue, red and green represent bcc, hcp and fcc atoms, respectively.

hindering the glide of preferential planes and the Shockley dislocation nucleations at low energies, can explain the resilience of W-hNPs to high temperatures. Both mechanisms are the first precursors of the collapse of fcc hNPs [63, 64, 74].

The thermal stability of these structures is an issue that can only be completely elucidated with dedicated experiments, but MD simulations can also provide some valuable information. We performed five independent simulations at 2500 K, lasting 10 μs each (*i.e.* much longer than usual simulations) to study the temperature-driven collapse, surface reconstruction or grain growth. Figure 6(*a*) illustrates the average potential energy (*U*) of a W-hNP. The potential energy does not vary for times longer than 1.5 μs, indicating the stability of the W-hNP. Recently, similar curves have been employed to demonstrate the thermal stability of polycrystalline hNPs (smaller than the ones analysed in this paper), which are affected by grain boundary coarsening [75]. Snapshots in figure 6(*b*) show that the cavity is preserved at 2500 K and that the variation in the potential energy is mainly due to surface atom rearrangement. It is important to note that high-temperature driven collapse has already been reported in other hollow nanostructures based on Pt, Au or MgO [76], thus the elevated thermal resistance shown by the W-hNPs can be attributed to the high melting point of W-based materials.
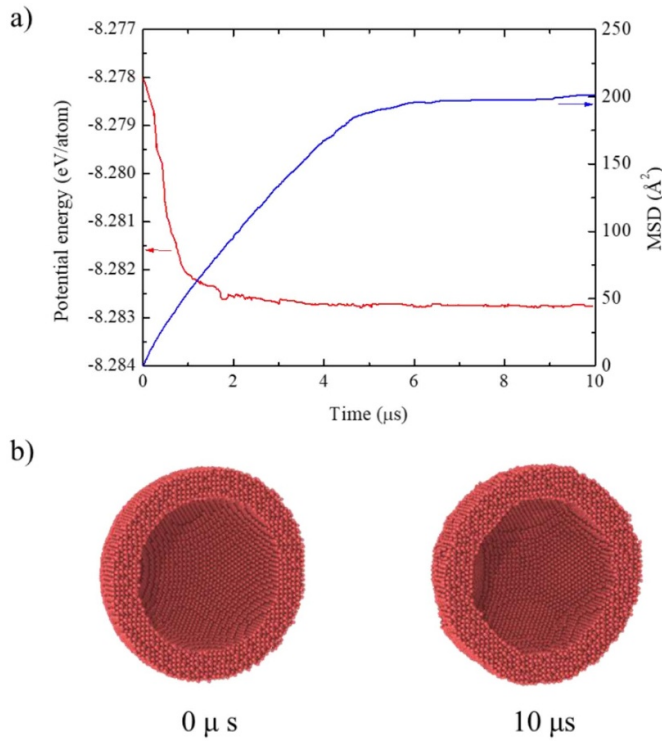
Figure 6. (a) Potential energy and mean square displacement (MSD) of a W-hNP kept at 2500 K for 10 μs. The curves were constructed averaging five independent simulations. (b) Illustration of a half cut of the hNP before and after the heating process.

Additionally, the mean square displacement (MSD) is included in figure 6(*a*), and is defined as:

$$\text{MSD} = \frac{1}{N} \sum_{i=1}^{N} \left[(x_i(t) - x_i(t=0))^2 + (y_i(t) - y_i(t=0))^2 + (z_i(t) - z_i(t=0))^2 \right],$$

(3)

where N is the number of atoms, and x_i, y_i and z_i are the coordinates as a function of time of the ith atom. The MSD initially increased almost linearly for the first 5 μs, but further on, the MSD remained stable. The initial increase indicates that the system evolved by means of a process of surface reconstruction and faceting without evidence of shrinkage (in agreement with the snapshots), while the later stabilization allows us to discard any significative atomic motion which could subsequently trigger the collapse of the structure. To quantify the atomic motion, a diffusion coefficient was computed from the MSD as $D = \frac{1}{6t} MSD(t)$. The atomic motion during the reconstruction rendered a diffusion coefficient of 5.8×10^{-10} cm^2 s^{-1} (for $t < 4$ μs), slightly higher than the surface self-diffusion coefficient of bulk W reported for the same temperatures, but rather low as expected due to the spherical shape of the W-hNP, which provides stability to the W-hNPs. In a microsecond time scale, discontinuities in physical parameters such as the MSD, the diffusion coefficient, and the potential energy provide information regarding drastic events, such as collapse, coalescence or reconstruction. The smooth
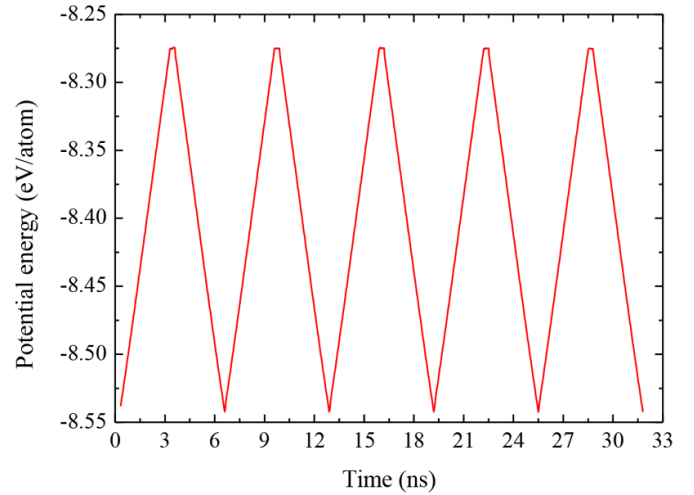

Figure 7. Potential energy of a W-hNP during five thermal load cycles. The temperature was raised from 300 to 2000 K in 3 ns, then held at 2000 K for 0.3 ns and returned to 300 K in 3 ns. Remarkably, the potential energy does not vary from cycle to cycle.

behaviour observed is a good indication of the structural integrity and thermal resilience of the hNP.

In order to use hNPs for FW applications, it is necessary to assess their thermal load resistance. This is related to the stability issues just discussed. Thus, dedicated experiments must be carried out for validation purposes with thermal load cycles of relevance in the context of the described fusion scenarios. In this work, we carried out MD simulations to study a W-hNP subject to several thermal load cycles. The potential energy evolution is shown in figure 7. The system was heated and cooled during five successive cycles, in which the temperature was raised from 300 K to 2000 K in 3 ns, kept at that value for the following 0.3 ns, and finally cooled down again to 300 K in 3 ns. Remarkably, the potential energy minima and maxima do not vary from cycle to cycle. In addition, the slopes from minimum to maximum and from maximum to minimum do not differ, which shows that the thermal loads are not inducing any structural collapse. These results indicate a good thermal load resistance of hNPs subject to sudden temperature ramps. The subtleties of long-term real experiments cannot be captured by our simulations, but they provide a reliable idea about the good behaviour of W-hNPs subject to thermal loads.

Upon irradiation, the fraction of incoming He ions that end up becoming captured in the inner cavity, either by direct implantation or through diffusion from the shell, is very significant. Obviously, the fraction captured depends on the energy of the incoming ions. In figure 9(*a*) we observe that at least 40 eV is required to implant the He atoms directly in the cavity (ions backscattered at the outer surface are ignored and 1000 effective implantations were considered for each energy, to get reliable curves). The maximum efficiency is achieved in the range of 40–200 eV, with ~35% of the ions trapped inside the cavity. Note that the captured fraction remains constant even at 200 eV. This is remarkable considering that the ion range obtained by SRIM calculations [31] is large enough to cross radially the whole W-hNP. However, if the He ions penetrate
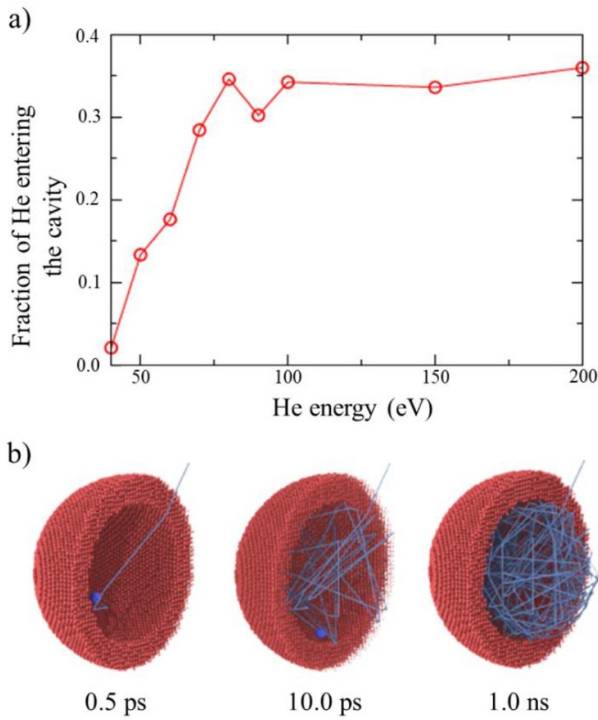
Figure 8. (a) Fraction of helium ions captured inside the hNP at different ion energies. (b) Illustration of ion capturing inside the cavity at the indicated times. For illustrative purposes, a half-cut of the hNP is displayed. Red dots represent the W atoms and blue lines the He trajectories.

Figure 9. Rupture of a hNP due to the excessive pressure caused by the access of He atoms (in blue) to the inner cavity at 3000 K.

Table 2. Rupture conditions in terms of temperature, He entering the cavity and inner pressure reached before rupture (determined following equation (2)).

Temperature (K)	Number of He atoms in the cavity prior to rupture	Inner pressure (GPa)
300	52 100	10.5
1000	48 900	7.5
2000	37 500	6.7
3000	32 000	5.5

the W-hNP shell a fraction of the kinetic energy is lost by different scattering mechanisms, including effective interactions with He atoms already captured in the cavity. Once inside the cavity, the energy of the incoming ion drops to only a few tens of eV. This energy loss translates into an increase of the reflection coefficient to almost 1.0 (full reflection) when impacting the inner wall of the W-hNP; thus, the He ion becomes captured inside the cavity. As a comparison, an ion with energy in the range 50 to 200 eV has a reflection coefficient close to 0.6–0.9 [22, 77, 78]. He atoms are slowly thermalized in the cavity via consecutive collisions with the inner surface, remaining in gas state as shown in the figure 8. It is interesting to note that in the case of pressurized cavities a significant part of the ion energy is transferred to the gas in the cavity, not producing damage to the W material. This is also true for high-energy ions during their passage across many W-hNPs.

Since the He formation energy in W is higher than 6 eV, the probability that a He atom captured as cavity gas will escape is very small. This is true even for very high temperatures near the melting point. Considering that the most relevant events in ICF and MCF are pulsed, high temperatures are only reached for a small fraction of a second in every pulse, reducing to a negligible value the fraction of captured He able to escape from the cavity. In this situation, it is very important to study the W-hNP behaviour when the cavity is pressurized. Figure 9 shows an example of the behaviour of a W-hNP when an excessive number of He atoms enters the
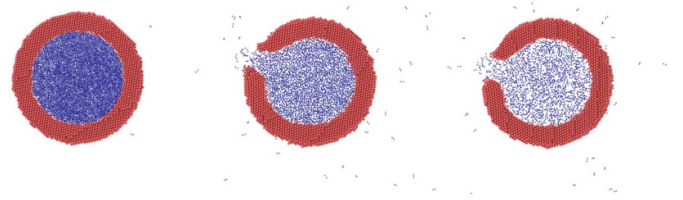
cavity, raising the inner pressure and causing the rupture of the NP. The W-hNP is able to resist very high internal pressures; however, rupture is produced at certain pressure depending on the temperature. Table 2 shows the relevant values; the pressure was calculated by means of equation (2). At room temperature, W-hNP rupture is produced at 10.5 GPa. This value decreases with increasing temperature to 5.5 GPa at 3000 K, which corresponds to 32 000 atoms in our W-hNPs. Despite the rupture pressure being roughly half of that at room temperature, it remains very high at 3000 K. Going to the fusion scenarios, in MCF the capture of tens of thousands atoms in the cavity occurs very rapidly, because the low-energy ions from the intense plasma discharge are implanted in roughly a monolayer of W-hNPs. In the case of ICF, He ions have high energies, therefore, cavity pressurization is a slow process. According to table 1, the maximum He filling rate is around 0.1 (0.04) He/pulse for the *Demo* (*Prototype*) scenarios. This means that 320 000 (1 066 667) pulses are needed in order to reach 32 000 atoms in the cavity. It may seem a large number but at a typical repetition rate of 10 Hz, this can be achieved in around 9 (30) hours, actually a very short time compared to the lifetime of a power plant. The situation is very different for hydrogen isotopes (D + T debris ions) because the formation energy of these isotopes in W is low (1–2 eV) [79, 80] to the extent that unlike the He case, captured D and T easily escape from the hNP cavity at the temperatures reached during the pulsed irradiation events.

The effective capture of He leads to NP rupture, which at first sight is a major concern for the use of W-hNPs in fusion applications. However, a careful study suggests that rupture is not always the final fate of the NPs. Contrary to the situation in MCF scenarios, where an abrupt pressure rise occurs in just one pulse, figure 10 shows that a gentle pressure increase (ICF scenarios) leads to the formation of an opening through which
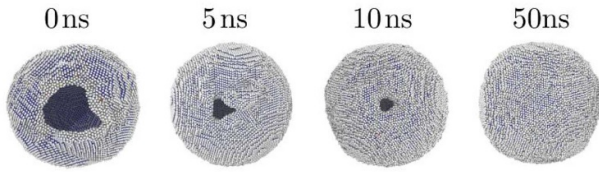
Figure 10. Example of self-healing process that leads to the recovery of a pressurized hollow NP at a constant temperature of 3000 K during 50 ns after the appearance of the opening. For illustrative purposes, the He atoms were deleted in the figure.
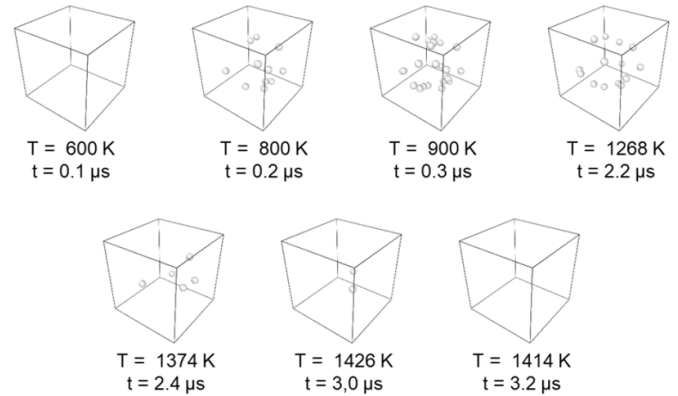

Figure 11. OKMC simulations of a hollow NP subject to stricter conditions than those expected in the ICF approach under the *Prototype* scenario. The temperature was varied according to figure 3 for NPs at a depth of 5.5 μm. In the first 500 ns, 2 He ions and 22 vacancies were introduced in the NP. In addition, 3 H ions were added during the first 2 μs.

gas atoms escape, reducing the pressure in the cavity. Next, the opening gradually closes in a few nanoseconds, recovering the original situation with a nearly perfect W-hNP containing some gas. Considering the specific example of a hNP at 3000 K, the escape of the gas results in a dramatic reduction in the cavity pressure from 5.5 to 0.5 GPa during the first nanosecond. The opening closes subsequently, in less than 50 ns, restoring a perfect W-hNP. Importantly, the remaining He pressure is too low to introduce detrimental tensile stress in the hNP shell. The results show that, under ICF scenarios, the W-hNPs behave as a self-regulating pressure device due to this extraordinary self-healing mechanism. According to figure 3, W-hNPs cannot operate under the *Demo* scenario because the peak temperature considerably exceeds the W melting point. However, under the *Prototype* scenario the use of W-hNPs for the FW turns out to be a promising solution.

4.2. Ion irradiation-induced damage evolution in hollow NPs

In the previous section, we concluded that a FW made of W-hNPs is promising for the ICF approach under the *Prototype* scenario because, according to our simulations, the hNPs turn out to be resistant to the temperature and pressure conditions. However, this is not enough to guarantee the survival of the FW. In the case of bulk tungsten, the damage generated by irradiation is the ultimate limit for the survival of the FW [6]. Hence, the role of irradiation damage must be studied for the case of a FW made of W-hNPs. For this purpose, we concentrated on the model cases shown in table 1. The defect generation and evolution in a hollow NP at a depth of 5.5 μm was simulated with the OKMC code MMonCa. This depth was chosen because it is where the maximum He implantation and He-induced vacancy concentration is expected, as shown in figure 2. The temperature evolution was taken from figure 3. Considerably stricter irradiation conditions than those of the *Prototype* scenario (table 1) were used to recreate adverse conditions as e.g. neutron irradiation or the arrival of high-energy hydrogen isotopes. Thus, instead of 0.04 He/hNP, we implanted 2 He ions in the first 500 ns and instead of 1.3 He-induced vacancies/hNP we included 22 vacancies. Furthermore, although the D/T range and the He range do not overlap, we implanted 3 H ions during the first 2 μs. Note that we would expect only 0.9 D + T/hNP in the *Prototype* scenario and at a depth of ∼2.5 μm.

Figure 11 depicts the results, showing only the defects in the shell. Ions can easily escape through the surfaces due to

their high mobility. For this reason, neither He nor H atoms are visible. On the other hand, we can observe the vacancy incorporation to the shell and their easy annihilation as the temperature increases. Hence, no vacancies remain in the hNP at the end of the cycle, once the temperature of the W-hNP is again at the base temperature. Vacancies, including those decorated with He and H, are very mobile at elevated temperatures and the outer and inner surfaces of the particle are so extremely close that the vacancy nucleation is suppressed. Therefore, the hNPs are unaltered by irradiation and, consequently, their mechanical properties are not expected to change much. In other words, unlike a FW made of bulk W, a FW made of hNPs is promising under relaxed ICF conditions (*Prototype* scenario). The ability to withstand the harsh temperature and pressure conditions and, even more importantly, to maintain integrity in spite of atomistic processes, reveals an inherent self-healing behaviour, very useful for nuclear applications in hostile irradiation conditions. We show next that, from the atomistic point of view, astonishingly, the hNPs can even resist the extreme conditions expected in MCF.

The situation in the MCF approach is completely different. We have already shown that the sudden ion discharge in the first layer of W-hNPs leads to pressurization and rupture, invalidating the use of hNPs against plasma discharges onto the divertor. However, it is instructive to ignore this fact and study irradiation damage in the MCF relaxed ITER scenario described in section 2.3 (ELM discharges of 3500 MW m^{-2} with a pulse duration of 0.2 ms). We followed defect evolution in a W-hNP with OKMC simulations. Assuming an ion energy of 50 eV and a <1% He content of the plasma, we obtain a He fluence <9 × 10^{16} cm^{-2} on the hNPs that cover the divertor. The backscattered fraction is ∼50% according to SRIM and MD. Therefore, for the considered hNPs (projected area 176.7 nm^2) we obtain ∼7 × 10^4 He/hNP in every ELM discharge event. It is actually a huge number, particularly if we recall that the number of D or T ions expected per ELM is around two orders of magnitude higher. Figure 4 contains the
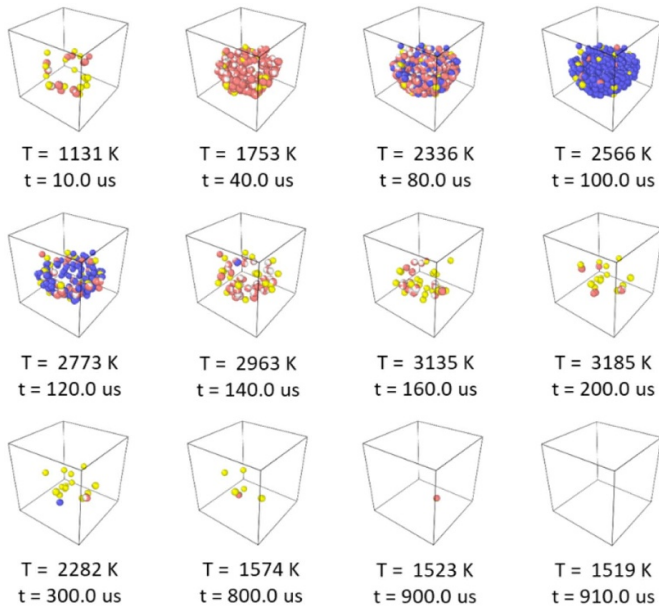
Figure 12. OKMC simulations of a hollow NP on the surface of the ITER divertor subject to an ELM in a relaxed scenario, *i.e.* discharges of 3500 MW m^{-2} resulting in the implantation of $\sim70 \times 10^3$ low-energy He ions in 200 μs. The temperature evolution follows figure 4. White spheres correspond to vacancies, red spheres to He atoms, yellow spheres to HeI clusters and blue spheres to HeV clusters.

temperature evolution in the relaxed ITER scenario and figure 12 the results of the OKMC simulations. We can observe how the huge number of He ions populate the hNP shell. The high He density at elevated temperatures leads to the formation of Frenkel pairs. Thus, many HeI clusters are visible (shown in yellow in figure 12). These clusters are mobile and annihilate at the surfaces releasing He, leaving behind vacancies, which are swiftly populated by incoming He ions. At 2566 K, HeV clusters are clearly visible (blue). Since the temperature continues to increase, despite the fact that the mobility of these clusters is not high, they can reach the surfaces and annihilate releasing He, or otherwise dissociate releasing a highly mobile He atom and a vacancy. At higher temperatures and during the cooling down we observe that all the remaining defects escape. Obviously, in these simulations we are not considering the expected hNP rupture due to the huge overpressure. However, it is interesting to observe the highly efficient self-healing mechanism that leads to a total restoration of the hNP after such a severe irradiation. This is our most important finding for the development of fusion materials for plasma-facing applications, considering that most attempts to develop suitable materials face unsolved issues related to irradiation damage, precisely where hNPs excel by exhibiting an extraordinary resistance.

5. Discussion

As mentioned in the introduction, one of the bottlenecks in the design of nuclear fusion power plants is related to the lack

of materials able to withstand the hostile conditions expected during operation. Hence, the fusion community has devoted important efforts to developing new radiation-resistant materials. In the case of plasma-facing applications, materials survivability is ultimately related to irradiation damage [6], which negatively affects macroscopic properties and leads to failure. In this paper, we have discussed a new approach based on a new type of material: hollow NPs. There have been reports about their good properties [38, 39, 46]. In this paper, we have studied their behaviour under extreme temperatures, thermal load cycles, pressure and irradiation conditions in different fusion scenarios. MCF conditions are the most severe ones, although we have considered ITER relaxed conditions in the divertor, not actual power-plant conditions. The high ion fluxes expected in pulsed events such as ELMs lead to unacceptably high temperatures and high ion concentrations. Thus, our hypothetical FW made of closely packed hNPs will not work in MCF power plants. On the other hand, for ICF with low-yield (50 MJ) direct-drive targets, a FW composed of hNPs exhibits an outstanding performance. These NPs resist very high temperatures and pressures, as well as thermal load cycles, and show extraordinary self-healing properties that assure total defect annihilation after every irradiation pulse. The self-healing behaviour takes place because the defects in the hNP shell can easily migrate to the outer or inner surface and annihilate, restoring the original hNP configuration. Gas atoms can be stored in the inner cavity, which has at least three positive effects: (i) the trapped gas atoms contribute to stop incoming ions without creating defects; (ii) they contribute to increase the overall thermal conductivity; and (iii) certain gas pressure in the cavity helps to maintain the hNP integrity at high temperatures, *i.e.* the gas avoids that the cavity closes and eventually disappears. However, excess pressure leads to hNP rupture, which in the MCF scenarios means the ultimate failure of the structure due to the sudden arrival of many ions. On the other hand, ions are captured very gently in ICF scenarios, producing an opening in the particle wall that relieves the pressure and closes afterwards, restoring the hNP configuration. This is another expression of the remarkable hNP self-healing properties.

These findings need experimental support but, once the good performance of the NPs has been confirmed experimentally, we can establish the basis of a route for materials development with enhanced radiation resistance properties. Experiments must also be used to study unaddressed aspects, like the role of the gas trapped in the cavity to reduce radiation damage and increase thermal conductivity, the synergies between damage induced by both He and H isotopes and the variation of the thermal properties of the ensemble of hNPs as a function of temperature and during irradiation. We made calculations on temperature evolution using conservative values for the thermal conductivity. However, irradiation effects and the generation of internal pressures can lead to contact loss between NPs with fatal consequences for heat release.

It is interesting to note that the solution based on a FW made of hNPs is promising for the case of low-yield targets (*Prototype* scenario). In principle, high-yield targets are attractive because they enable power plants with a high nominal power at

a low repetition rate. However, not only this study, but also previous ones on FWs and others on final lenses [81], indicate that from the point of view of materials integrity, the use of high-yield targets with the present state of the art will lead to excessively large chambers with the consequent cost increments and additional engineering needs. This suggests that future full-scale power plants may demand strategies based on low-yield targets with higher repetition rates in compact chambers, similar to those currently being developed for small modular reactors. Indeed, laser systems are flexible enough to operate with several small chambers in a natural way.

We have not addressed the practical realization of a FW made of hNPs. Instead, we considered an ensemble of close-packed hNPs with good contact to assure good thermal conductivity. A practical realization requires further efforts to determine whether the ensemble can be directly grown by existing methods [82], or if there exist appropriate surfactants able to withstand the irradiation conditions. Alternatively, practical realizations can be based on closed-pore, nanometre wall foams with regularly located open channels for gas release.

6. Conclusions

By means of MD and OKMC simulations, we studied the behaviour of W-hNPs (7.5 and 5.0 nm external and internal radius, respectively) under different ICF and MCF nuclear fusion scenarios. The simulations show that the W-hNPs are able to withstand very high temperatures ($\sim$3000 K) and huge internal pressures (>5 GPa at this temperature) before rupture occurs. Interestingly, a gentle pressure increase, as in ICF irradiation, does not produce W-hNP rupture but the appearance of an opening in the particle wall which enables the release of the trapped gas; subsequently, the opening closes in a few nanoseconds, restoring the initial hNP. This constitutes an efficient self-healing mechanism for pressure relief that prevents hNP rupture. There is yet another self-healing mechanism to eliminate the irradiation damage (the ultimate problem for PFMs), which takes place because the defects in the hNP shell easily reach the internal or external surfaces at the operation temperatures, where they annihilate. Thanks to this behaviour, the W-hNPs are able to withstand the relaxed ICF scenario (*Prototype*). The situation in MCF divertor scenarios is very different. The huge fluxes of low-energy ions lead to a sudden rise of light species concentration at the surface of the FW. As a result, hNPs would simply explode due to extreme overpressurization. However, even in this scenario of large discharges, the W-hNPs would be able to recover radiation damage due to He irradiation, which proves the good radiation resistance properties of W-hNPs. If our findings are experimentally proven, new routes to PFM development can be explored based on the principles behind the extraordinary resistance of the hNPs, in particular, to irradiation damage, which is the long-term unsolved problem of PFMs.

The development of a new class of material with enhanced radiation resistance properties has important implications for power-plant design. As discussed here, these new materials will be beneficial not only for plasma-facing applications, but also for other components in nuclear facilities that can take advantage of them for improved designs. Despite the promising good properties reported in this paper, we are still concerned about the very extreme conditions that materials must face in nuclear fusion facilities. It is not clear whether solutions can be found for all the expected scenarios (e.g. realistic MCF power-plant conditions, not discussed in this paper). This enforces the need for team work to find solutions based on a combination of smart strategies and materials development. The final designs will be a compromise dependent upon what can be achieved in different fields, one of them materials resistance. For example, in this sense, we mentioned in this paper our concern about the use of high-yield targets with realistic-sized chambers and recalled suggestions made by others about the advantages of low-yield targets, which would require power-plant strategies similar to those under development for modular reactors.

ORCID iDs

Pablo Díaz-Rodríguez https://orcid.org/0000-0003-4162-4699
Francisco Munoz https://orcid.org/0000-0002-4324-8650
Ovidio Peña-Rodríguez https://orcid.org/0000-0002-7329-0550

References

[1] Windsor C. 2019 Can the development of fusion energy be accelerated? An introduction to the proceedings *Phil. Trans. R. Soc. Lond.* A **377** 20170446
[2] Linke J., Du J., Loewenhoff T., Pintsuk G., Spilker B., Steudel I. and Wirtz M. 2019 Challenges for plasma-facing components in nuclear fusion *Matter Radiat. Extrem.* **4** 056201
[3] Donné A.J.H. 2019 The European roadmap towards fusion electricity *Phil. Trans. R. Soc. Lond.* A **377** 20170432
[4] Nygren R.E., Youchison D.L., Wirth B.D. and Snead L.L. 2016 A new vision of plasma facing components *Fusion Eng. Des.* **109–111** 192–200
[5] Alvarez J., Rivera A., Gonzalez-Arrabal R., Garoz D., Del R.E. and Perlado J.M. 2011 Materials research for HiPER

laser fusion facilities: chamber wall, structural material and final optics *Fusion Sci. Technol.* **60** 565–9

[6] Garoz D., Páramo A.R., Rivera A., Perlado J.M. and González-Arrabal R. 2016 Modelling the thermomechanical behaviour of the tungsten first wall in HiPER laser fusion scenarios *Nucl. Fusion* **56** 126014

[7] Roth J. *et al* 2009 Recent analysis of key plasma wall interactions issues for ITER *J. Nucl. Mater.* **390–391** 1–9

[8] Latkowski J.F. *et al* 2011 Chamber design for the laser inertial fusion energy (LIFE) engine *Fusion Sci. Technol.* **60** 54–60

[9] Hassanein A. and Morozov V. 2002 Chamber wall response to target implosion in inertial fusion reactors: new and critical assessments *Fusion Eng. Des.* **63–64** 609–18

[10] Tokheim R.E., Curran D.R., Seaman L., Cooper T., Anderson A.T., Burnham A.K., Scott J.M., Latkowski J. and Schirmann D. 1999 Hypervelocity shrapnel damage assessment in the nif target chamber *Int. J. Impact Eng.* **23** 933–44

[11] Petzoldt R.W. *et al* 2002 Direct drive target survival during injection in an inertial fusion energy power plant *Nucl. Fusion* **42** 1351–6

[12] Craxton R.S. *et al* 2015 Direct-drive inertial confinement fusion: a review *Phys. Plasmas* **22** 110501

[13] Blanchard J.P. and Raffray R. 2007 Laser fusion chamber design *Fusion Sci. Technol.* **52** 441

[14] Norimatsu T., Shimada Y., Furukawa H., Kunugi T., Nakajima H., Kajimura Y., Tsuji R., Yoshida H. and Mima K. 2009 Activities on the laser fusion reactor KOYO-F in Japan *Fusion Sci. Technol.* **56** 361–8

[15] Ogawa Y. 2016 Fusion studies in Japan *J. Phys. Conf. Ser.* **717** 012003

[16] Böhne D. 1982 A conceptual design study of a heavy-ion driven inertial confinement fusion power plant *Nucl. Eng. Des.* **73** 195–200

[17] Najmabadi F. *et al* 2004 Operational windows for dry-wall and wetted-wall IFE chambers *Fusion Sci. Technol.* **46** 401–16

[18] Allain J.P. 2002 Erosion from liquid-metal plasma-facing components in future fusion devices *AIP Conf. Proc.* **635** 273

[19] Philipps V. 2011 Tungsten as material for plasma-facing components in fusion devices *J. Nucl. Mater.* **415** s2–9

[20] Buzi L., De Temmerman G., Huisman A.E., Bardin S., Morgan T.W., Rasinski M., Pitts R.A. and Van Oost G. 2017 Response of tungsten surfaces to helium and hydrogen plasma exposure under ITER relevant steady state and repetitive transient conditions *Nucl. Fusion* **57** 126009

[21] Hammond K.D. 2017 Helium, hydrogen, and fuzz in plasma-facing materials *Mater. Res. Express* **4** 104002

[22] Johnson P. and Mazey D. 1978 Helium gas bubble lattices in face-centered-cubic metals *Nature* **276** 595–6

[23] Gilbert M.R., Dudarev S.L., Nguyen-Manh D., Zheng S., Packer L.W. and Sublet J.-C. 2013 Neutron-induced dpa, transmutations, gas production, and helium embrittlement of fusion materials *J. Nucl. Mater.* **442** S755–60

[24] Soltan A., Vassen R. and Jung P. 1991 Migration and immobilization of hydrogen and helium in gold and tungsten *J. Phys. D: Appl. Phys.* **70** 793–7

[25] Allain J.P. 2019 Alternative plasma-facing-material concepts for extreme plasma-burning nuclear fusion environments *Fusion Sci. Technol.* **75** 702–18

[26] Ackland G. 2010 Controlling radiation damage *Science* **327** 1587–8

[27] Beyerlein I.J., Caro A., Demkowicz M.J., Mara N.A., Misra A. and Uberuaga B.P. 2013 Radiation damage tolerant nanomaterials *Mater. Today* **16** 443–9

[28] Valles G., Panizo-Laiz M., González C., Martin-Bragado I., González-Arrabal R., Gordillo N., Iglesias R., Guerrero C.L., Perlado J.M. and Rivera A. 2017 Influence of grain boundaries on the radiation-induced defects and hydrogen in nanostructured and coarse-grained tungsten *Acta Mater.* **122** 277–86

[29] El-Atwani O., Hattar K., Hinks J.A., Greaves G., Harilal S.S. and Hassanein A. 2015 Helium bubble formation in ultrafine and nanocrystalline tungsten under different extreme conditions *J. Nucl. Mater.* **458** 216–23

[30] El-Atwani O., Hinks J.A., Greaves G., Gonderman S., Qiu T., Efe M. and Allain J.P. 2014 In-situ TEM observation of the response of ultrafine- and nanocrystalline-grained tungsten to extreme irradiation environments *Sci. Rep.* **4** 4176

[31] Renk T.J., Provencio P.P., Tanaka T.J., Olson C.L., Peterson R.R., Stolp J.E., Schroen D.G. and Knowles T.R. 2005 Chamber wall materials response to pulsed ions at power-plant level fluences *J. Nucl. Mater.* **347** 266–88

[32] Sharafat S., Ghoniem N.M., Anderson M., Williams B., Blanchard J. and Snead L. 2005 Micro-engineered first wall tungsten armor for high average power laser fusion energy systems *J. Nucl. Mater.* **347** 217–43

[33] Renk T.J., Williams B., El-Guebaly L. and Jaber A. 2011 Three-dimensional 'textured' coatings as first-wall materials: exposure to energetic ions on RHEPP-1 *Fusion Sci. Technol.* **60** 570–8

[34] Renk T.J., Provencio P.P., Tanaka T.J., Blanchard J.P., Martin C.J. and Knowles T.R. 2012 Survivability of first-wall materials in fusion devices: an experimental study of material exposure to pulsed energetic ions *Fusion Sci. Technol.* **61** 57–80

[35] Gao E., Nadvornick W., Doerner R. and Ghoniem N.M. 2018 The influence of low-energy helium plasma on bubble formation in micro-engineered tungsten *J. Nucl. Mater.* **501** 319–28

[36] Gao E., Doerner R., Williams B. and Ghoniem N.M. 2019 Low-energy helium plasma effects on textured micro-porous tungsten *J. Nucl. Mater.* **517** 86–96

[37] Qin W., Ren F., Doerner R.P., Wei G., Lv Y., Chang S., Tang M., Deng H., Jiang C. and Wang Y. 2018 Nanochannel structures in W enhance radiation tolerance *Acta Mater.* **153** 147–55

[38] Aradi E., Lewis-Fell J., Harrison R.W., Greaves G., Mir A.H., Donnelly S.E. and Hinks J.A. 2018 Enhanced radiation tolerance of tungsten nanoparticles to He ion irradiation *Nanomaterials* **8** 1052

[39] González R.I., Valencia F., Mella J., van Duin A.C.T., So K.P., Li J., Kiwi M. and Bringa E.M. 2016 Metal-nanotube composites as radiation resistant materials *Appl. Phys. Lett.* **109** 033108

[40] Andersen M., Sharafat S. and Ghoniem N. 2006 Thermo-mechanical analysis of a micro-engineered tungsten-foam armored IFE FW *Fusion Eng. Des.* **81** 1639–45

[41] Shiryaev A.A. *et al* 2018 Ion implantation in nanodiamonds: size effect and energy dependence *Sci. Rep.* **8** 5099

[42] Shan Z.W., Adesso G., Cabot A., Sherburne M.P., Syed Asif S.A., Warren O.L., Chrzan D.C., Minor A.M. and Alivisatos A.P. 2008 Ultrahigh stress and strain in hierarchically structured hollow nanoparticles *Nat. Mater.* **7** 947–52

[43] Valencia F.J., González R.I., Vega H., Ruestes C., Rogan J., Valdivia J.A., Bringa E.M. and Kiwi M. 2018 Mechanical properties obtained by indentation of hollow Pd nanoparticles *J. Phys. Chem.* C **122** 25035–42

[44] Valencia F.J., Pinto B., Kiwi M., Ruestes C.J., Bringa E.M. and Rogan J. 2020 Nanoindentation of polycrystalline Pd hollow nanoparticles: grain size role *Comput. Mater. Sci.* **179** 109642

[45] Yang W., Yang J., Dong Y., Mao S., Gao Z., Yue Z., Dillon S.J., Xu H. and Xu B. 2018 Probing buckling and post-buckling deformation of hollow amorphous carbon nanospheres: in-situ experiment and theoretical analysis *Carbon* **137** 411–8

[46] Xie L., Zheng J., Liu Y., Li Y. and Li X. 2008 Synthesis of Li$_2$ NH hollow nanospheres with superior hydrogen storage kinetics by plasma metal reaction *Chem. Mater.* **20** 282–6

[47] Valencia F.J., González R.I., Tramontina D., Rogan J., Valdivia J.A., Kiwi M. and Bringa E.M. 2016 Hydrogen storage in palladium hollow nanoparticles *J. Phys. Chem.* C **120** 23836–41

[48] Alvarez J., Gonzalez-Arrabal R., Rivera A., Del Rio E., Garoz D., Hodgson E.R., Tabares F., Vila R. and Perlado M. 2011 Potential common radiation problems for components and diagnostics in future magnetic and inertial confinement fusion devices *Fusion Eng. Des.* **86** 1762–5

[49] Solórzano E., Rodríguez-Perez M.A. and de Saja J.A. 2009 Thermal conductivity of metallic hollow sphere structures: an experimental, analytical and comparative study *Mater. Lett.* **63** 1128–30

[50] Bhatt S., Kumar R. and Kumar M. 2017 Specific heat and thermal conductivity of nanomaterials *Mod. Phys. Lett.* B **31** 1750011

[51] Anon ARIES Web Site – Aries IFE Documents (http://aries.ucsd.edu/ARIES/WDOCS/ARIES-IFE/)

[52] Ziegler J.F., Ziegler M.D. and Biersack J.P. 2010 SRIM – the stopping and range of ions in matter (2010) *Nucl. Instrum. Methods Phys. Res.* B **268** 1818–23

[53] Zhong Y., Nordlund K., Ghaly M. and Averback R.S. 1998 Defect production in tungsten: a comparison between field-ion microscopy and molecular-dynamics simulations *Phys. Rev.* B **58** 2361

[54] Raffray A.R., El-Guebaly L., Federici G., Haynes D., Najmabadi F. and Petti D. Team AIFE 2004 Dry-wall survival under IFE conditions *Fusion Sci. Technol.* **46** 417–37

[55] Plimpton S. 1995 Fast parallel algorithms for short-range molecular dynamics *J. Comput. Phys.* **117** 1–19

[56] Daw M.S. and Baskes M.I. 1984 Embedded-atom method: derivation and application to impurities, surfaces, and other defects in metals *Phys. Rev.* B **29** 6443–53

[57] Ackland G.J. and Thetford R. 1987 An improved N-body semi-empirical model for body-centred cubic transition metals *Philos. Mag.* A **56** 15–30

[58] Juslin N. and Wirth B.D. 2013 Interatomic potentials for simulation of He bubble formation in W *J. Nucl. Mater.* **432** 61–66

[59] Marinica M.-C., Ventelon L., Gilbert M.R., Proville L., Dudarev S.L., Marian J., Bencteux G. and Willaime F. 2013 Interatomic potentials for modelling radiation defects and dislocations in tungsten *J. Phys.: Condens. Matter* **25** 395502

[60] Bonny G., Grigorev P. and Terentyev D. 2014 On the binding of nanometric hydrogen–helium clusters in tungsten *J. Phys.: Condens. Matter* **26** 485001

[61] Beck D.E. 1968 A new interatomic potential function for helium *Mol. Phys.* **14** 311–5

[62] Ziegler J.F. and Biersack J.P. 1985 The stopping and range of ions in matter *Treatise on Heavy-Ion Science* ed D.A. Bromley (New York: Springer) pp 93–129

[63] Reyes P.N., Valencia F.J., Vega H., Ruestes C., Rogan J., Valdivia J.A. and Kiwi M. 2018 The stability of hollow nanoparticles and the simulation temperature ramp *Inorg. Chem. Front.* **5** 1139–44

[64] Jiang L., Yin X., Zhao J., Liu H., Liu Y., Wang F., Zhu J., Boey F. and Zhang H. 2009 Theoretical investigation on the thermal stability of hollow gold nanoparticles *J. Phys. Chem.* C **113** 20193–7

[65] Larsen P.M., Schmidt S. and Schiøtz J. 2016 Robust structural identification via polyhedral template matching *Model. Simul. Mater. Sci. Eng.* **24** 055007

[66] Stukowski A. 2010 Visualization and analysis of atomistic simulation data with OVITO—the open visualization tool *Model. Simul. Mater. Sci. Eng.* **18** 015012

[67] Stukowski A. 2012 Structure identification methods for atomistic simulations of crystalline materials *Model. Simul. Mater. Sci. Eng.* **20** 045021

[68] Martin-Bragado I., Rivera A., Valles G., Gomez-Selles J.L. and Caturla M.J. 2013 MMonCa: an object kinetic Monte Carlo simulator for damage irradiation evolution and defect diffusion *Comput. Phys. Commun.* **184** 2703–10

[69] Valles G., González C., Martin-Bragado I., Iglesias R., Perlado J.M. and Rivera A. 2015 The influence of high grain boundary density on helium retention in tungsten *J. Nucl. Mater.* **457** 80–87

[70] Valles G., Martin-Bragado I., Nordlund K., Lasa A., Björkas C., Safi E., Perlado J.M. and Rivera A. 2017 Temperature dependence of underdense nanostructure formation in tungsten under helium irradiation *J. Nucl. Mater.* **490** 108–14

[71] Becquart C.S. and Domain C. 2009 An object kinetic Monte Carlo simulation of the dynamics of helium and point defects in tungsten *J. Nucl. Mater.* **385** 223–7

[72] Becquart C.S., Domain C., Sarkar U., DeBacker A. and Hou M. 2010 Microstructural evolution of irradiated tungsten: ab initio parameterisation of an OKMC model *J. Nucl. Mater.* **403** 75–88

[73] Huang R., Shao G.-F., Zeng X.-M. and Wen Y.-H. 2015 Diverse melting modes and structural collapse of hollow bimetallic core-shell nanoparticles: a perspective from molecular dynamics simulations *Sci. Rep.* **4** 7051

[74] Valencia F.J., González R.I., Valdivia J.A., Kiwi M., Bringa E.M. and Rogan J. 2017 Inducing porosity on hollow nanoparticles by hypervelocity impacts *J. Phys. Chem.* C **121** 17856–61

[75] Valencia F.J., Ramírez M., Varas A. and Rogan J. 2020 Understanding the stability of hollow nanoparticles with polycrystalline shells *J. Phys. Chem.* C **124** 10143–9

[76] Enyashin A.N. and Ivanovskii A.L. 2007 Structural, thermal properties and stability of monolithic and hollow MgO nanocubes: atomistic simulation *J. Mol. Struct. THEOCHEM* **822** 28–32

[77] Li M., Wang J. and Hou Q. 2012 Molecular dynamics studies of temperature effects on low energy helium bombardments on tungsten surfaces *J. Nucl. Mater.* **423** 22–27

[78] Borovikov V., Voter A.F. and Tang X.-Z. 2014 Reflection and implantation of low energy helium with tungsten surfaces *J. Nucl. Mater.* **447** 254–70

[79] Oda T., Zhu D. and Watanabe Y. 2015 Kinetic Monte Carlo simulation on influence of vacancy on hydrogen diffusivity in tungsten *J. Nucl. Mater.* **467** 439–47

[80] Heinola K. and Ahlgren T. 2010 First-principles study of H on the reconstructed W(100) surface *Phys. Rev.* B **81** 073409

[81] Páramo A.R., Sordo F., Garoz D., Garrec B.L., Perlado J.M. and Rivera A. 2014 Transmission final lenses in the HiPER laser fusion power plant: system design for temperature control *Nucl. Fusion* **54** 123019

[82] Zhang R. *et al* 2013 Soap-film coating: high-speed deposition of multilayer nanofilms *Sci. Rep.* **3** 1477